Article:
Abul, MR, Cochrane, RF and Mullis, AM (2022) Partitionless solidification and anomalous triradiate crystal formation in drop-tube processed Al-3.9 wt%Fe alloys. Materials Today Communications, 31. 103274. ISSN: 2352-4928

https://doi.org/10.1016/j.mtcomm.2022.103274

Partitionless Solidification and Anomalous Triradiate Crystal Formation in Drop-Tube Processed Al-3.9 wt%Fe Alloys

Mehmet R. Abul, Robert F. Cochrane & Andrew M. Mullis

School of Chemical & Process Engineering, University of Leeds, Leeds LS2 9JT, UK.

Abstract

Drop tube atomized Al-3.9 wt% Fe alloy has been investigated. Spherical samples were collected and sieved into 9 different size fractions ranging between 850+ μm to 38 μm, with corresponding estimated cooling rates ranging between 100 and 20,000 K s^{-1}. X-ray diffraction analysis showed the presence of Al, $Al_{13}Fe_4$ and Al_6Fe in all size fractions. Scanning electron microscopy and optical microscopy have been employed for microstructural evolution. Large proeutectic crystals of $Al_{13}Fe_4$ surrounded by α-Al, dendritic α-Al with interdendritic lamellar eutectic, lamellar eutectic and rod-like eutectic was observed in samples with d > 212 μm. In the smaller samples (d < 212 μm) primary $Al_{13}Fe_4$ disappeared and featureless Y-shaped structures with thin, triradiating arms start to emerge. These Y-shaped structures can be heavily fragmented in nature and appear to be the first phase to nucleate in the droplets, followed by divorced eutectic, microcellular α-Al, dendritic α-Al with lamellar interdendritic eutectic and lamellar and rod-like eutectics. Serial sectioning with a cumulative depth of 20.2 μm has revealed that the Y-shaped features have an internally connected sheet-like morphology. Transmission electron microscopy reveals that these Y-shaped features are composed of nano-sized needle-like and spherical precipitates. TEM diffraction from a Y-shaped region has revealed the presence of Al_mFe in this region. EDX analysis shows that these Y-shaped features have the same bulk composition as the liquid from which they grew, suggesting they form via partitionless solidification of highly supersaturated α-Al, which subsequently undergoes solid-state decomposition. The formation of these feature also slightly increases the eutectic spacing from 0.35 μm in the 300-212 μm size fraction to 0.45 μm in the 212-150 μm size fraction. In order to understand the effect of nonequilibrium the solidification on the mechanical properties microhardness of the droplets was measured. The microhardness has risen from 50 $HV_{0.01}$ to 83 $HV_{0.01}$ for $850 +$ μm and $53 \leq d \leq 38$ μm droplets respectively.

Keywords: Al-Fe alloys, non-equilibrium containerless solidification, drop tube, microstructure, metastable phases, microhardness.

1. Introduction

Al alloys are widely recycled and, as a result, impurity elements such as Fe are inevitably present in such recycled scrap[1]. The presence of Fe has detrimental effects on the mechanical properties of aluminium alloys[2]. Moreover, it is hard and costly to remove iron from aluminium. However, Rapid Solidification (RS) processing allows the modification of deleterious effects by extending solid solubility, refining grain size and favouring the formation of metastable phases including, at very high cooling rates, quasicrystalline and amorphous phases[3–5]. Furthermore, RS processed Al-Fe alloys have potential for high temperature applications[6] due to the formation of metastable intermetallic phases such as Al_6Fe, Al_5Fe_2, Al_mFe (m=4.0 to 4.4), Al_xFe (x=5.0 to 5.5) and Al_9Fe_2[3,7,8], with the phase(s) formed depending on the cooling rate and degree of undercooling. For example, while Al_mFe forms at relatively high cooling rates, Al_xFe exists at lower cooling rates[9]. Moreover, the formation of Al_6Fe requires moderate cooling rate[9]. Therefore, the cooling rate and degree of undercooling plays a critical role in phase selection in Al-Fe alloys. Furthermore, the final microstructure is also process dependent. Among the available RS methods, drop-tube processing remains a leading technique, combining both high cooling rates and deep undercooling. Such undercooling arising as drop-tube processing is a containerless technique, with solidification taking place during free-fall, wherein potential heterogeneous nucleation sites are avoided[10,11]. Moreover, drop-tube processing is also a good analogue for commercial powder metallurgical production techniques, such as gas atomization.

RS processing of Al-Fe alloys has been of significant interest as it provides considerable microstructural and constitutional changes. For example, RS studies[12,13] on Al-8 wt% Fe have shown that while large powders show the formation of both primary $Al_{13}Fe_4$ and Al-$Al_{13}Fe_4$ eutectic, decreasing the powder size, and thus increasing the cooling rate, promoted the formation of Al-Al_6Fe eutectic over Al-$Al_{13}Fe_4$. Moreover, the microstructure shifted from coarse cellular α-Al to fine microcellular α-Al with increasing cooling rate. Similar results have also been reported in drop-tube atomized Al-3.6 wt% Fe alloy[14]. Although these alloys are all hypereutectic with respect to the Al-$Al_{13}Fe_4$ eutectic, at the higher cooling

rates studied α-Al was the primary solidification phase. It is likely this is because the Al-$Al_{13}Fe_4$ eutectic coupled zone, which is heavily skewed towards the intermetallic side, can be by-passed via deep undercooling. A recent re-evaluation of the Al-$Al_{13}Fe_4$ coupled zone is presented in [15]. Electromagnetic levitation (EML) studies[7] on the Al-8 wt% Fe alloy have shown the formation of what the authors describe as primary star-like $Al_{13}Fe_4$, together with the formation of metastable Al-Al_mFe and Al-Al_xFe (x = 5) eutectics beyond an undercooling of 155 K.

Henein et al.[16] studied the microstructural evolution of impulse atomized, hypoeutectic Al-0.61 wt% Fe and hypereutectic Al-1.90 wt% Fe droplets with sizes ranging from 925 µm to 231 µm, with corresponding cooling rate between 20 K s^{-1} and 10000 K s^{-1}. They observed the formation of $Al_{13}Fe_4$, Al_6Fe and Al_5Fe_2 intermetallics in large powders (d > 550 µm), whilst smaller powders displayed an unresolved intermetallic. Chen et al.[8] later studied the same alloys using TEM and neutron diffraction, finding the unresolved intermetallic to be Al_mFe. Moreover, Henein et al.[16] performed 3D X-ray micro-tomography upon a 550 µm droplet of this alloy, revealing the formation of a large, needle-like, primary phase with branches along the whole of its length. This they reported as an α-Al crystal radiating outwards from a single nucleation point. Similar microstructures were reported in impulse atomized Al-5 wt% Cu and Al-17 wt% Cu, with droplet diameters ranging between 400 µm 710 µm[17]. Samples showed multiple equiaxed crystallites spreading across the droplet, radiating from a single point, inferred to be the nucleation site. However, neither work provided detailed microstructural analysis of these regions to confirm that such regions were indeed α-Al.

The purpose of this study is to characterize rapidly solidified, drop-tube processed Al-3.9 wt% Fe alloy as a function of cooling rate. For this purpose, XRD, optical microscopy, Scanning Electron Microscopy (SEM) and Transmission Electron Microscopy (TEM) techniques were employed. In order to understand the effect of the cooling rate on the mechanical properties of the alloy, microhardness testing was performed.

2. Experimental Procedure

The Al-3.9 wt% Fe alloy was prepared using high purity Al (>99.99 wt%) and fine, high purity (99.9 wt%), iron wires. These were placed in a high vacuum furnace and melted at a temperature of 1200 °C for 30 minutes. The alloy was then slowly cooled to room

temperature, following which the ingot was sectioned and mounted in resin. XRD analysis, optical microscopy and SEM were employed upon the mounted and polished sample to confirm the complete dissolution of the iron wires.

The alloy was then placed in an alumina crucible with three laser drilled holes of 300 µm diameter in the base. The alumina crucible was then placed in a graphite susceptor around which two alumina heat shields were located. An R-type thermocouple was inserted into the crucible to measure the temperature of the sample. The crucible was then sealed to the top of the drop-tube where the sample was induction heated using a 3 kW RF power supply.

After the drop-tube was sealed, it was evacuated to a pressure of around 1 Pa and backfilled with dry, oxygen free, nitrogen gas to a pressure of 50 kPa. To remove any residual oxygen this process was repeated 3 times. A turbomolecular was employed for the final evacuation stage, wherein a pressure of 2.7 x 10^{-3} Pa was attained in the drop-tube, before filling to 40 kPa with nitrogen gas. The sample was then heated to 100 K above the alloys calculated liquidus temperature, after which ejection of the melt took place by pressurizing the crucible with 0.4 MPa of nitrogen.

After cooling, the spherical powders were collected from the bottom of the drop-tube and sieved in to 9 different sizes: 850+ µm, 850-500 µm, 500-300 µm, 300-212 µm, 212-150 µm, 150 -106 µm, 106-75 µm. 75-53 µm and 53-38 µm.

X-ray diffraction was conducted on the sieved samples using a Philips X'Pert Diffractometer with Cu K_α radiation and a step size of 0.033° between 2θ values of 20° to 80°. The samples were then hot mounted in resin, with the mounted samples being ground and polished for microscopic analysis. Grinding was performed using 800, 1200 and 2000 grit SiC papers progressively. The samples were then polished using 6 µm, 3 µm and 1 µm diamond pastes. To obtain a scratch free surface, a final polishing step was employed utilising 0.05 µm colloidal silica on a semiautomatic polisher for 1.5 minutes. The samples were washed in running water and methanol and then dried with a hot air blower between each of the grinding and polishing stages. The samples were etched using Keller's Reagent (1% HF, 1.5 % HCl, 2.5% HNO_3 and 95% water) for optical microscopy.

Etched samples were analysed under an Olympus BX51 optical microscope. The samples were then polished again and carbon coated for SEM analysis. An Hitachi Su8230 SEM and a Carl Zeiss EVO MA 15 SEM with built-in energy dispersive X-ray analyser (EDS) were used for SEM analysis. Transmission Electron Microscope (TEM) samples were cut using a

Focused Ion Beam (FIB) connected to FEI nova 200 NanoLab FEGSEM. The samples were later investigated using an FEI Titan3 Themis 300 TEM.

A Tukon™ 1202 Wilson Hardness (Vickers) testing machine, using 10g load at room temperature, was used on mounted and colloidal silica polished samples for microhardness measurements. For each droplet size range 10 measurements were made.

Serial sectioning, consisting of consecutive grinding, polishing and etching steps was conducted on one droplet from the 150-106 sieve fraction in order to reveal its internal 3D structure. The depth difference between consecutive sections was measured by using the microhardness machine. Before polishing, a microhardness indent was made on an area close to the region of interest on the sample. The average diagonal length, l, of the indent before and after polishing was measured and the change, Δl, calculated. The change in the depth of the sample, Δt, was calculated using the geometrical properties of Vickers microhardness indent as

$$\Delta t = \Delta l/7$$

After the change in the depth of the sample was measured, the sample was etched and investigated under OM.

Eutectic spacing was measured by drawing lines with a length, v, perpendicular to the lamellar eutectic and the number of lamellar eutectics, c, were count. The lamellar eutectic spacing, λ, were then determined by

$$\lambda = v/c$$

The image processing software ImageJ was used to determine the dendrite size and the volume fraction of the dendrites with distance from the arms of the Y-structures. For each linear segment of the Y the centre line was first identified and lines parallel to this drawn on either side at spacings of 5, 10, 15 and 20 μm. Contrast within the grey scale image was used to identify regions of ∝-Al from other phases present, wherein all regions of ∝ that were (say) between 10-15 μm from the arm of the Y could be identified and sized using automatically using the in-built functions within ImageJ, with the equivalent circular diameter, based upon the measure feature area being reported.

3. Results

3.1. Cooling rate estimation

Due to the small size of the drop-tube particles and that processing occurs with the droplets in free-fall, the thermal history of such particles cannot be measured directly. However, the cooling rate can be estimated using the heat balance of the solidifying droplets. The method for the estimation of the cooling rate is given elsewhere[15]. Figure 1 gives the cooling rates of the droplets as a function of their diameter. The cooling rate ranges between 150 K s^{-1} and 20,000 K s^{-1} for 850 µm and 38 µm samples respectively.

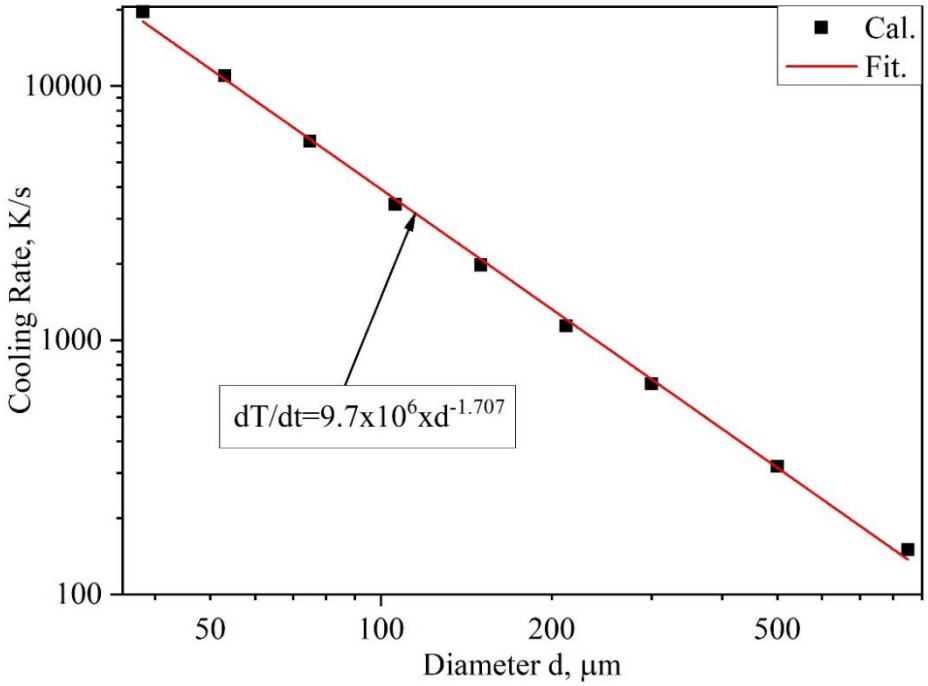

Figure 1: Estimated cooling rates of the droplets as a function of droplet diameter, *d*.

3.2. XRD Results

XRD patterns for selected size ranges, namely: 850-500, 212-150 and 75-53 µm, are given in Figure 2. These sample sizes are chosen to reflect the wide range of cooling rates available, with XRD for slow cooled, medium cooled and fast cooled samples being given. The XRD results show that there are three different phases in the samples regardless of their diameter, and thus their cooling rate. These phases are α-Al, $Al_{13}Fe_4$ and Al_6Fe. However, it should be noted that there is no PDF card in the database for Al_mFe and thus indexing for this phase has not taken place. Moreover, it is known from literature that Al_mFe[18] has many peaks in common with both Al_6Fe and $Al_{13}Fe_4$, making it notoriously difficult to index. In this regard,

the presented XRD data does not preclude Al_mFe being present within any of the samples studied, just that from the XRD data alone we cannot prove that it is present.

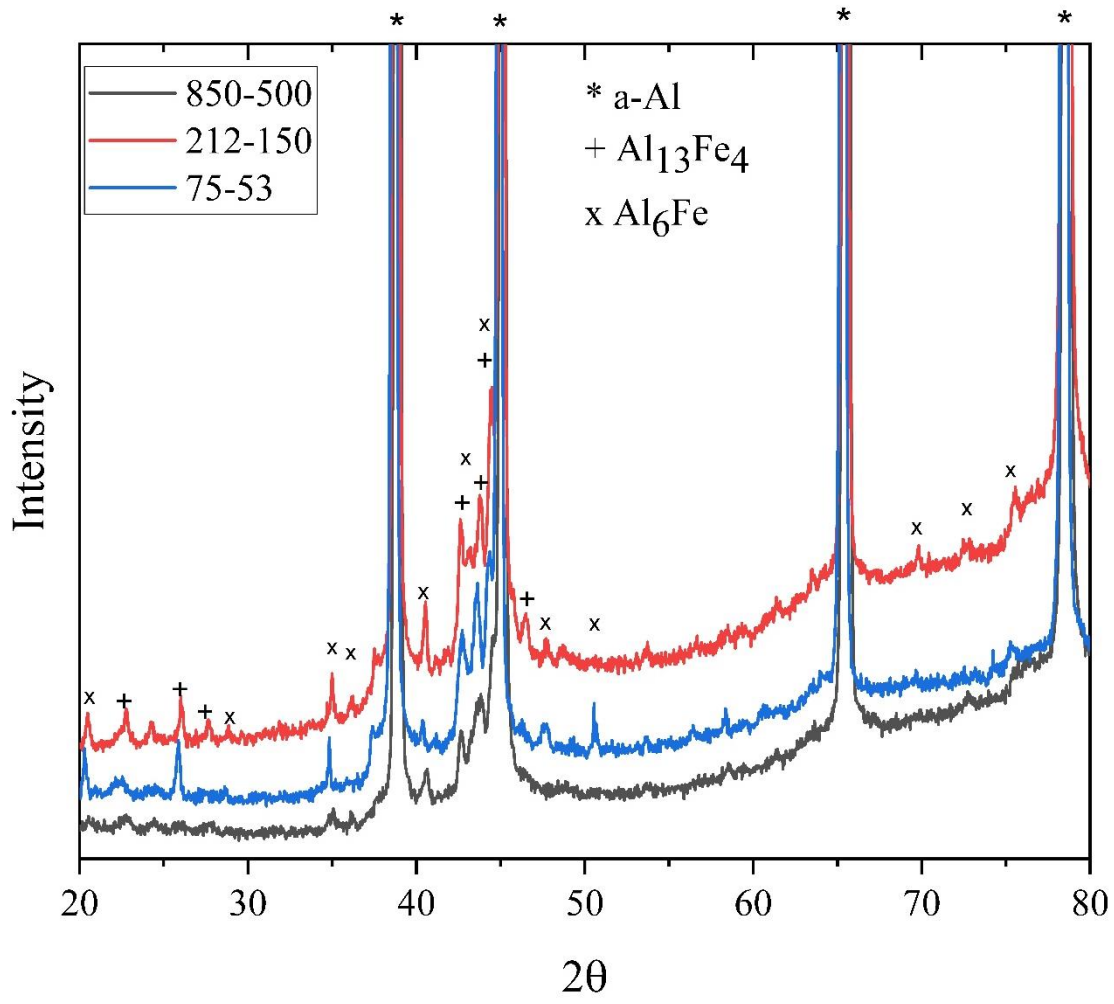

Figure 2: XRD results for 850-500, 212-150 and 75-53 µm samples.

3.3. Microstructure and phase identification

An SEM micrograph of the furnace cooled Al-3.9 wt% Fe sample, with an average cooling rate of around 20 K min^{-1} is shown in Figure 3. Due to the low cooling rate of the sample it appears to have solidified in accordance with the Al-Fe equilibrium phase diagram, the microstructure consisting of proeutectic $Al_{13}Fe_4$ and α-Al + $Al_{13}Fe_4$ eutectic. The proeutectic $Al_{13}Fe_4$ has a blocky, clover-like morphology and is embedded within a eutectic consisting of fine needles of $Al_{13}Fe_4$ in an α-Al matrix. This is the classical $Al_{13}Fe_4$ morphology, with the thin intemetallic needles being the phase which so disastrously impacts the properties of Fe-contaminated Al scrap.

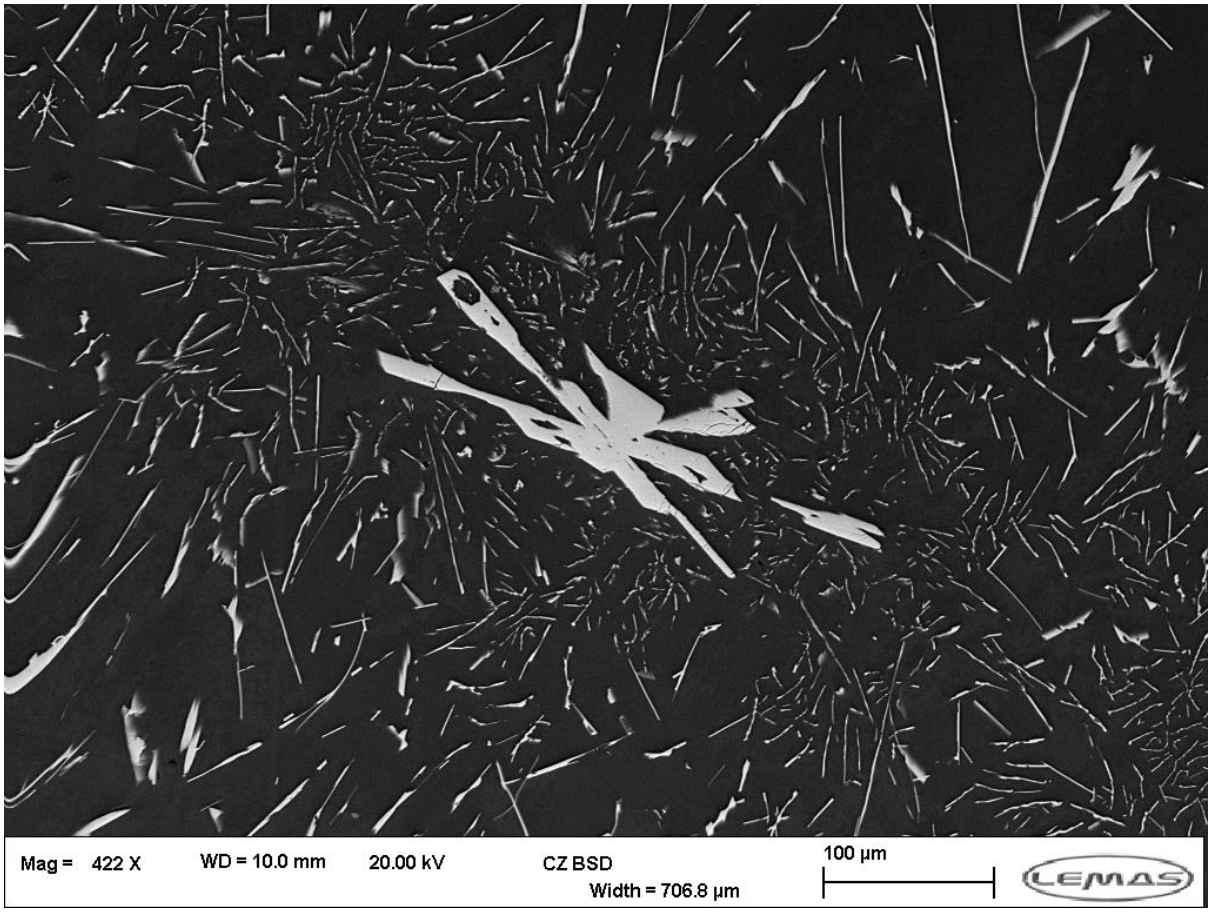

Figure 3: SEM micrograph of the furnace cooled sample depicting blocky proeutectic $Al_{13}Fe_4$, and Al-$Al_{13}Fe_4$ eutectic comprising fine needles of $Al_{13}Fe_4$ in an α-Al matrix.

Figure 4 shows optical micrographs of the largest (d > 850+ µm) drop-tube atomized sample. It is clear from Figure 4 that the microstructure of the sample is mostly eutectic. The sample consists of proeutectic $Al_{13}Fe_4$ surrounded by α-Al, together with a mixture of rod-like eutectic, lamellar eutectic and dendritic α-Al. As the sample size is large, with a correspondingly low cooling rate of around 100 K s^{-1} (based on an assumed diameter from the optical micrograph of 900 µm), coupled with a large (100 K) difference between the liquidus and eutectic temperatures, we would conclude there is sufficient time for the unconstrained growth of primary $Al_{13}Fe_4$. This is formed with either a compact clover-like morphology, as shown in Figure 4d wherein the crystal has a length of ~40 µm and a thickness of ~20 µm, or as an elongated collection of needles radiating from a single nucleation point, as in Figure 4c. In this latter case the agglomerate of needles has a length of 20-40 µm and a thickness of around 5-10 µm. As evident in Figure 4a, all of the primary $Al_{13}Fe_4$ crystallites are surrounded with α-Al, almost certainly due to depletion of Fe in the

melt surrounding the growing crystallites. A related phenomenon also appears to be visible in Figure 3 in which the eutectic surrounding the blocky proeutectic $Al_{13}Fe_4$ contains finer and shorter $Al_{13}Fe_4$ needles than that away from the proeutectic phase. It appears that in the drop-tube samples this Fe-depletion goes further and the surrounding melt solidifies as α-Al with insufficient Fe to form the eutectic.

Upon further cooling the temperature of the droplet will fall below the eutectic temperature, wherein most of the remaining liquid will be transformed into eutectic. Figure 4d shows that both rod-like and lamellar eutectic with different sizes and densities are present in the sample, and that these eutectics are divided by a distinct boundary. Our previous research[15] has shown that while the lamellar eutectic is Al-$Al_{13}Fe_4$, metastable Al-Al_6Fe eutectic adopts a rod-like structure. That is, both stable Al-$Al_{13}Fe_4$ and metastable Al-Al_6Fe eutectics are formed in the slowest cooled sample. Moreover, a long boundary structure radiating from the eutectic towards the α-Al can be seen in Figure 4d. A small amount of dendritic α-Al was also formed in the sample as shown in Figure 4b. For dendritic α-Al to be formed in a hypereutectic Al-Fe alloy, the temperature of the remaining melt must drop below that on the α-Al side of the coupled zone. Overall, the solidification sequence for these large droplets would appear to be (i) primary $Al_{13}Fe_4$, (ii) simultaneous growth of dendrites and eutectics (it is not clear from the Figure 4 which of the eutectics formed first nor where in this sequence the small regions of dendritic α-Al come) and (iii) interdendritic eutectic.

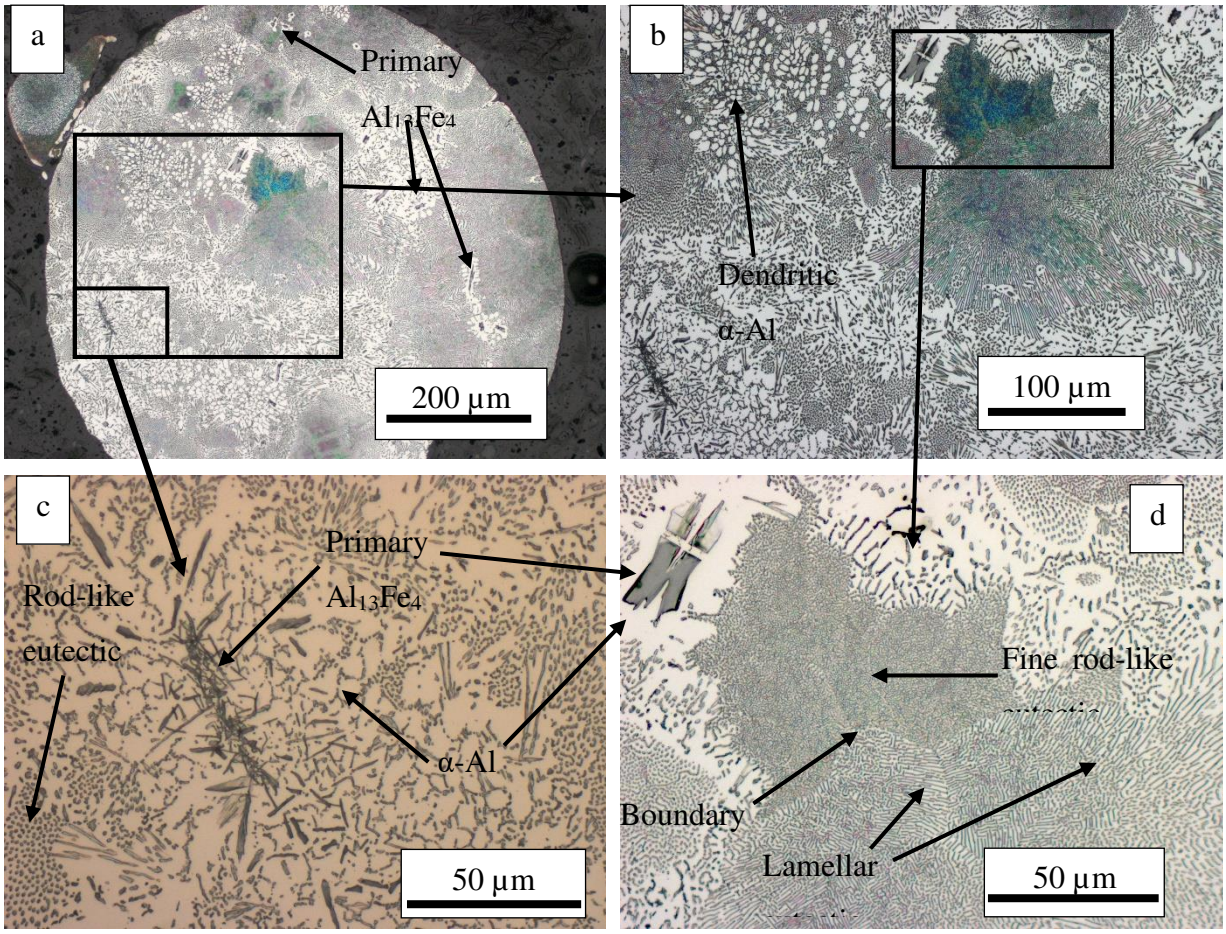

Figure 4: Microstructures of the rapidly solidified Al-3.9 wt% alloy with sample diameter of 850+ µm showing primary $Al_{13}Fe_4$, rod-like eutectic, lamellar eutectic, α-Al and dendritic α-Al.

The microstructures (for the sake of brevity not shown) of 850-212 µm samples were similar to the 850+ µm samples, being composed of proeutectic $Al_{13}Fe_4$, dendritic α-Al, rod-like eutectic and lamellar eutectic. However, decreasing the sample size below 212 µm results in a dramatic change in the microstructure. Figure 5 shows the microstructure of a 212-150 µm sample. The first point to note is that primary $Al_{13}Fe_4$, which, as shown in Figure 4, was observed in all samples with $d > 212$ µm, is no longer present in these smaller droplets. As the 212-150 µm sample experiences higher cooling rate, and thus higher undercooling than $d > 212$ µm droplets, the likelihood is that other, faster growing, phases become either thermodynamically or kinetically favoured over $Al_{13}Fe_4$.

The microstructure of the 212-150 µm sample is dominated by a region (highlighted with a dashed line) which appears to be featureless and which in many, but not all, micrographs appears as three thin arms radiating out from a single point (see e.g. Figure 9 which will be

discussed later). In order to adopt an unambiguous terminology, these featureless structures will be referred to as "Y-shaped structures", regardless of their geometry. The rest of the droplet microstructure consists of cellular α-Al, dendritic α-Al, lamellar eutectic and rod-like eutectic, with a broadly similar set of microstructures being observed in all samples with sizes smaller than 212 µm. Tracing outwards, normal to the featureless regions we note that the dendritic α-Al appears to grows out of Y-shaped structure, with the dendrite arms getting coarser moving away from the Y-shaped structure. This would be consistent with the Y-shaped structure being the first phase to form in the droplet, with further evidence for this being presented later. Moreover, although the Y-shaped features looks like a continuous phase, Figures 5c & d show that in some instances the arms have undergone significant fragmentation and spheroidisation, with such instances being indicated by the white arrows in the figure. The presence of cellular and dendritic α-Al between the fragments suggests that fragmentation took place whilst the rest of the sample was still liquid. Figure 5c shows that cellular α-Al nucleated on the Y-shaped structure and is followed by the formation of dendritic α-Al. Moreover, lamellar eutectic then formed in the interdendritic regions, as shown in Figure 5c and d. The angles between the arms of Y-shaped feature in Figure 5a was measured as 104°, 121° and 135° resepectively. Furthermore, EDX measurements (not shown) from the Y-shaped region show that its composition, to within the experimental error of the technique, is the same as that of the melt, Al-3.9 wt% Fe, for all droplet sizes. This is consistent with the Y-shaped morphology appearing somewhat lighted than the dendritic α-Al in the backscatter images and would imply that solidification of this phase was partitionless.

Moving further out from the featureless Y-shaped structures we observe a transition from dendritic to fully eutectic growth, which is likely to represent a decrease in undercooling occurring as a result of recalescence. The final stage of growth is therefore fully eutectic, as shown in Figure 5b. It is clear from figure 5b that there are both lamellar and rod-like eutectics present in the droplet. While the lamellar eutectic formed close to the dendritic region, the formation of rod-like eutectic took place away from the dendritic area and, consequently, away from Y-shaped structure where nucleation was initiated. This could tentatively be taken as evidence that the Al_6Fe rod-like eutectic formed subsequent to the lamellar $Al_{13}Fe_4$ eutectic, although such a conclusion would be surprising as $Al_{13}Fe_4$ is the stable phase and Al_6Fe the metastable phase. As the undercooling of the droplet would be expected to drop during recalescence, we would normally expect the growth of the metastable

phase to precede that of the stable phase in the solidification sequence. We will return to this point in the Discussion section.

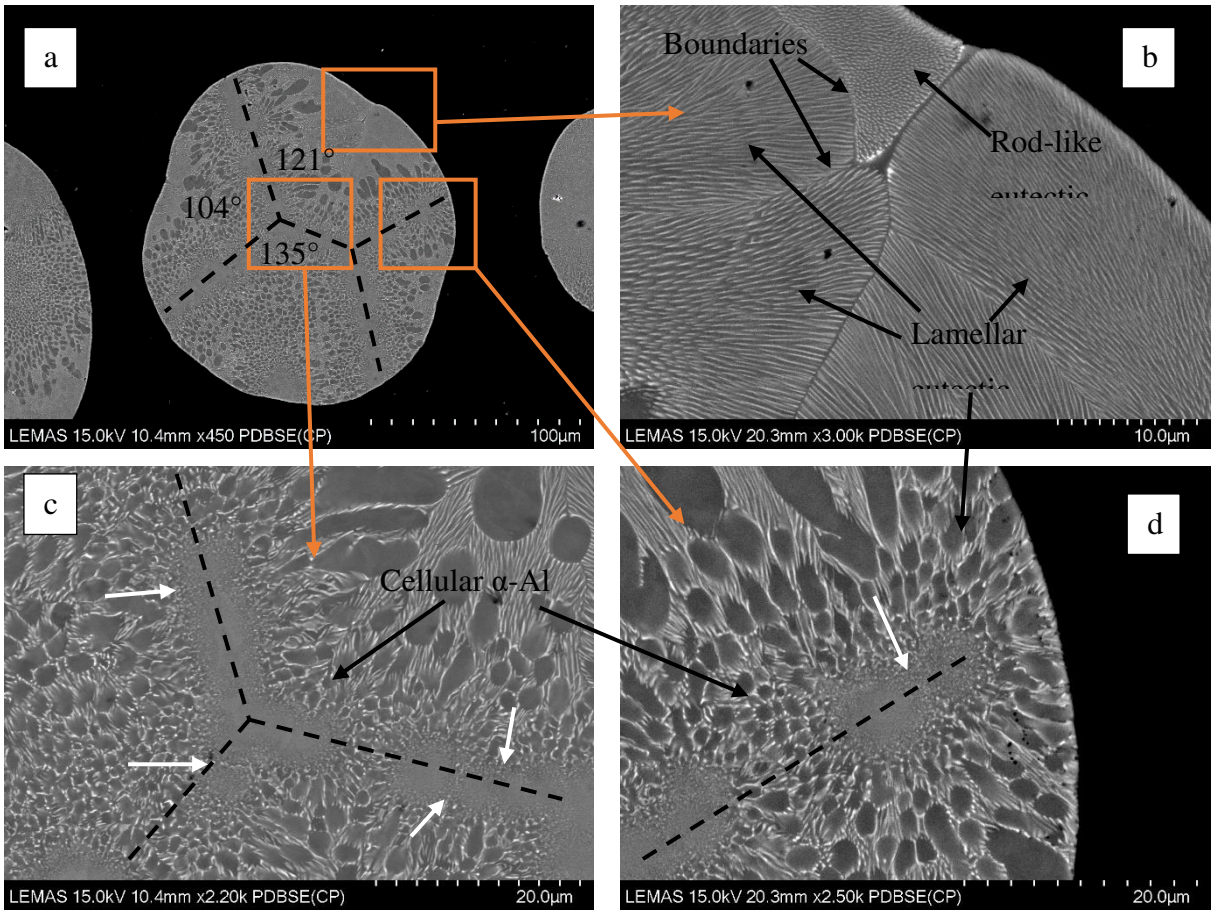

Figure 5: SEM micrographs of 212-150 µm sample showing Y-shaped phase, cellular α-Al, dendritic α-Al, interdendritic lamellar eutectic, lamellar eutectic and rod-like eutectic. (white arrows show the fragmented Y-shaped phase and dashed black lines show the structure of Y-shaped)

These featureless Y-shaped structures were observed in all powders with d < 212 µm and displayed a number of different morphologies. Figure 6 shows OM micrographs of the different morphologies of Y-shaped structure formed in 150-106 µm droplets. While the Y-shaped structure in Figure 6a & e are similar to the one in Figure 5a, Figures 6b & c show more complex structures, with Figure 6b displaying a closed pentagonal morphology. It will be demonstrated below, via serial sectioning, that such closed shapes can be generated out of the Y-shaped crystals observed in Figures 5 and 6a & c. Figure 6c also shows the secondary branching of a Y-shaped feature, as indicated by the dashed lines in the figure. While the angles between the first branches of the Y-morphology shown in Figure 6c is close to 120°, the angle between the secondary branches was measured as around 60°. However, moving

away from the Y-shaped features the solidification sequence appears similar to the other droplets, with the formation of α-Al, lamellar & rod-like eutectic and an interdendritic lamellar eutectic. The angles between the arms of Y-shaped features can adopt a number of values as given in the figure. The angles in the upper part of the Y-shaped feature shown in Figure 6a for example, are close to 120°, ranging between 114° and 124°. However, the angles between the lower arms range between 146° and 81°. Moreover, three near right angles and two 135° angles were measured in the pentagon given in Figure 6b.

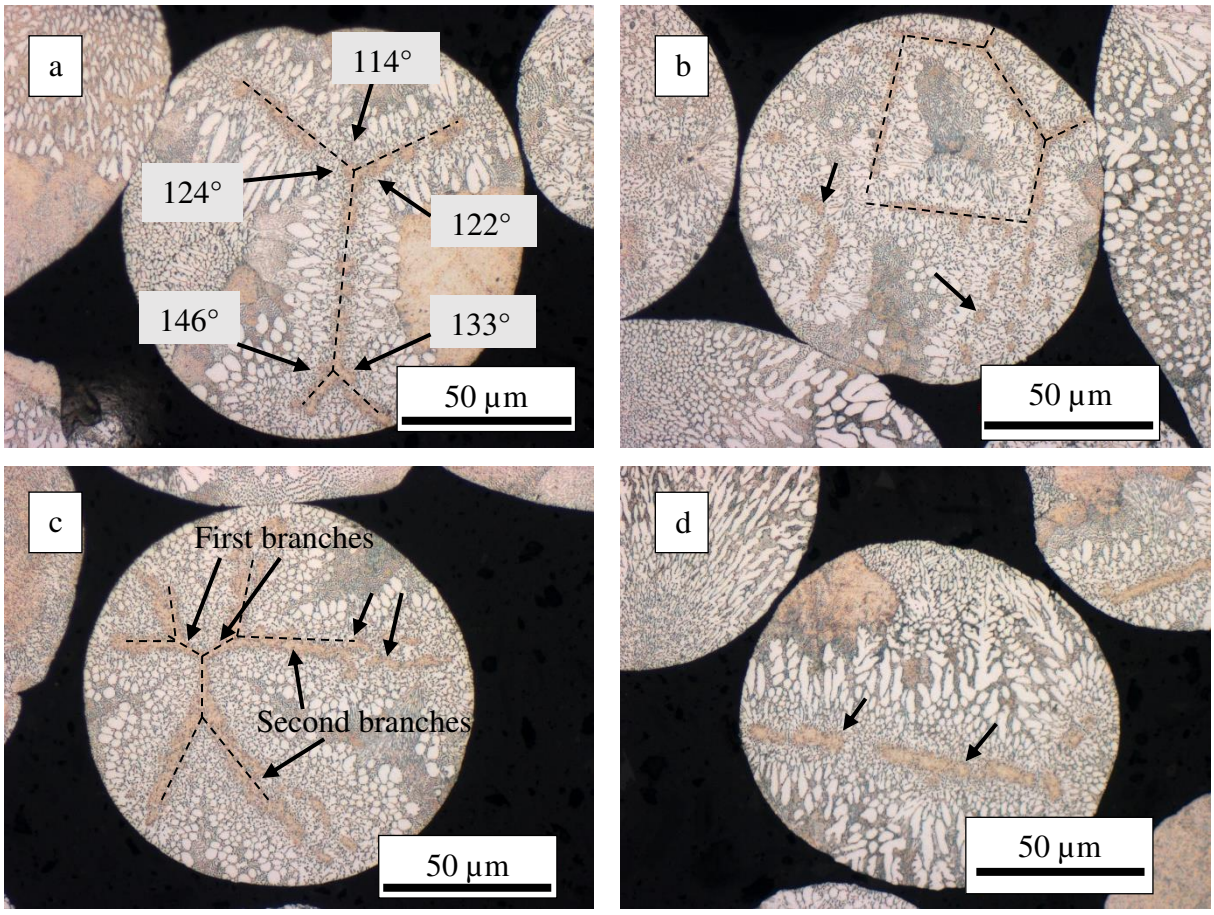

Figure 6: OM micrographs of 150-106 µm sample depicting different morphologies of featureless Y-shaped structure.

Figure 7 shows the microstructures of selected 106-75 µm droplets. Figure 7a shows an unusual sample which has clearly been impacted by a smaller satellite particle with an apparent diameter of around 38 µm. The larger droplet here shows distinct deformation at the impact point, together with signs of a meniscus in the contact zone, suggesting it was at least partially liquid at the point of impact. Conversely, the smaller droplet has retained a well-

defined circular outline, suggesting it was fully solid at the point of impact. This would seem entirely plausible given the much higher cooling rates of these small droplets. Y-shaped structures are evident in both droplets and a similar featureless material, although not displaying the Y-shaped structure, is also apparent in the larger droplet at the impact site. Our conclusion would be that the satellite acted as a heterogenous nucleation site for the larger sample, forming the very fine structure observed. Interestingly, the Y-shaped structure in the larger droplet is not obviously connected to the impact region. There are three possible explanations: (i) the regions are connected, but the connection is not visible as it is not in the plane of the section, (ii) the regions are not connected, the Y-shaped feature nucleated independently after impact, (iii) the regions are not connected, the Y-shaped feature had already nucleated prior to impact but the impact region was still liquid. All appear possible and there does not appear any definitive means to decide between the alternatives. Assuming the featureless material that comprises the Y-shaped features and the impact region is a high undercooling phase, as seem probable, we would judge possibility (iii) less likely than (i) or (ii) above, as the latent heat evolved in forming a Y-shaped feature prior to impact would have lowered the overall undercooling of the droplet somewhat.

The angles between Y-shaped features in the large droplet in Figure 7a have been measured and range between 108° and 137°. As can be seen in the figure, and in line with other samples, the dendritic α-Al gets coarser away from the Y-shaped feature. The sizes of dendritic α-Al were measured 5, 10, 15, 20 µm away from Y-shaped and found as 1.05, 1.6, 2.6 and 3.3 µm, respectively. Moreover, the volume fraction of dendritic α-Al was measured to be decreasing away from the Y-shaped features, wherein the volume fraction of α-Al decreases from 80 vol% at 10 µm from the arms of the Y-shaped feature (measured normal to the arms) to 72 vol% at 20 µm from the Y. All of this factors point decisively to the featureless material of bulk composition 3.9 wt% Fe being the first material to solidify.

However, in some droplets this featureless material has a much more dendritic character, an example of which is shown in Figures 7b-d. Divorced eutectic is formed in the regions close to arms radiating out from a common point (Figure 7b). This later transitioned in to cellular α-Al and then dendritic α-Al. Moreover, Figure 7d shows the formation of spherical and needle-like precipitates in the middle of arms, perfectly aligned parallel to the arms. The diameter of spherical precipitates was measured as ~200 nm, while the needle-like precipitates have a length of ~500 nm and a thickness around 100 nm. It is not clear whether the featureless material nucleated on these fine precipitates, which would therefore be a

precursor primary phase, or whether they subsequently precipitated from the featureless phase. Given their strong linear alignment, it would seem likely that if they did grow direct from the melt, that this was as a single, extended feature which has subsequently fragmented and undergone partial spheroidisation.

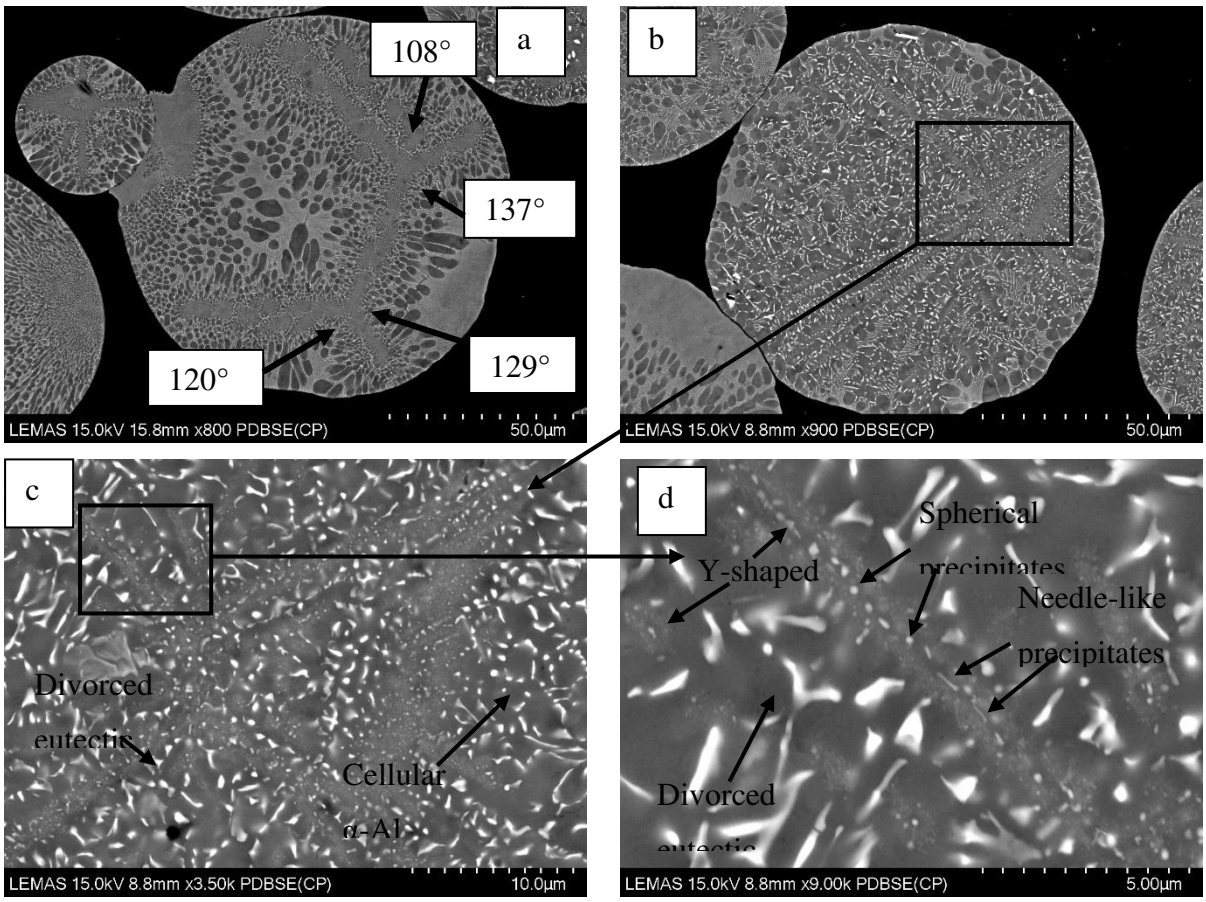

Figure 7: SEM micrographs of the 106-75 µm samples depicting featureless Y-shaped structure.

Increasing the cooling rate appears to increase the volume fraction of the Y-shaped structure in the samples and, as a result, that of the eutectic and α-Al is decreased. This can be seen from Figure 8, which shows the microstructure of selected 75-53 µm and 53-38 µm samples. In some cases the featureless material displays a clear Y-shaped morphology (Figure 8d), in other a clearly dendritic morphology, albeit with non-orthogonal side branching (Figures 8a & b) and in yet other a morphology intermediate between the two.

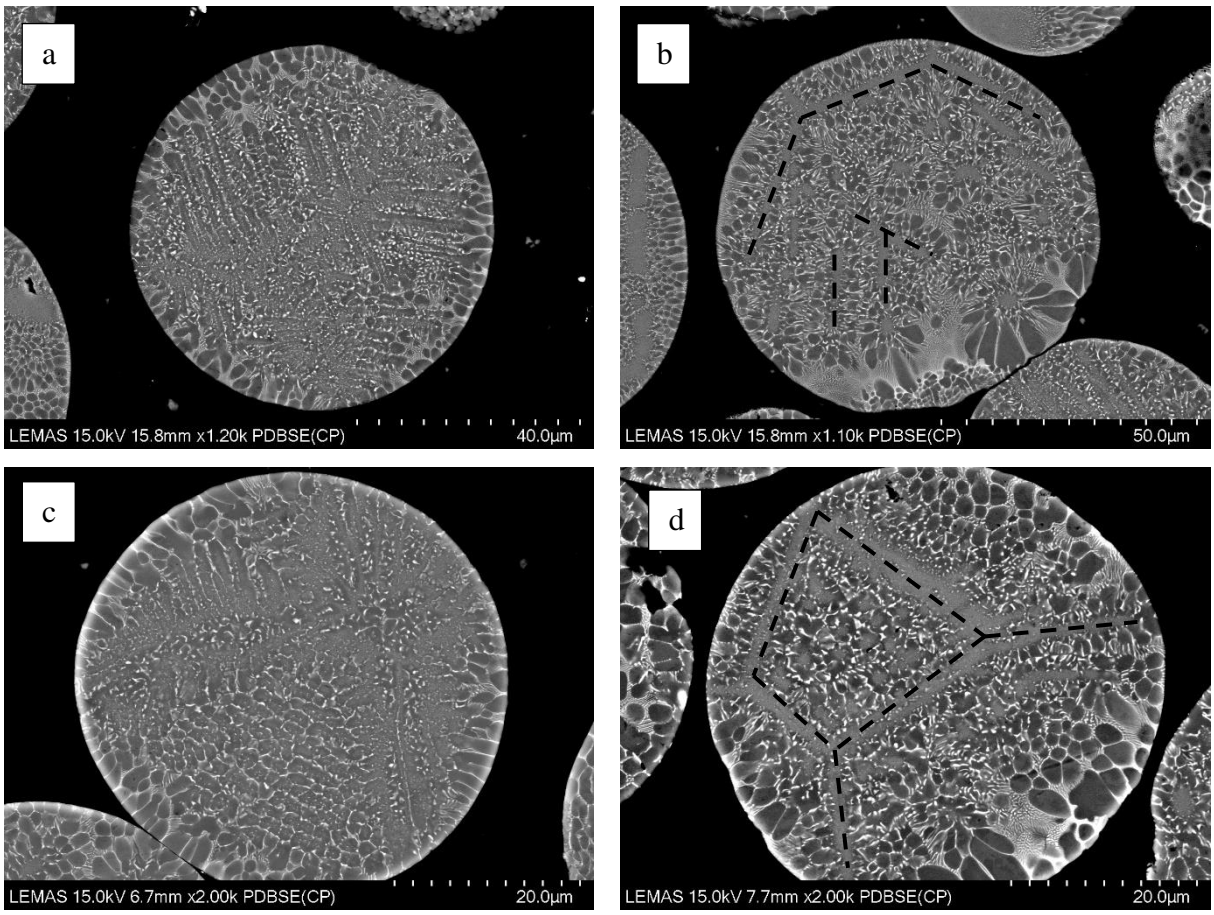

Figure 8: SEM micrographs of a) and b) 75-53 µm samples c) and d) 53-38 µm samples

3D structure of Y-shaped phase

As seen from the above figures, the Y-shaped features can adopt a number of different morphologies. However, it is not clear how these structures are internally connected. Thus, consecutive polishing and etching was performed on a single droplet from the 150-106 µm sieve fraction in order to reveal the 3D structure of a Y-shaped feature, with a total cumulative depth of 20.2 µm being removed. The results are given in Figure 9, with the sectioning depth given in the insert box. As with other samples, it is clear from the figures that dendritic α-Al gets coarser away from the Y-shaped feature in all sections. Figures 9 a-g show a simple Y-shaped structure, albeit that one of the arms (toward the bottom of the sample as oriented in the figure) has split into two secondary branches.

The latter parts of the figure (Figures 9h-k) demonstrate how the Y-shaped feature transitions into a closed shape (in this case a kite shaped quadrilateral). A new branch emerges towards

the lower left of the sample and joins with one of the exiting secondary arms, forming the observed closed shape. This demonstrates that a closed form can originate from a three armed "Y" and we believe a similar argument can be applied to the pentagon shown in Figure 6b. The angles between the arms of Y-shaped feature are given in the figure, these being 144°, 96° and 120° in the first cross section. While the 144° angle does not change with the change in depth, the other angles do progressively change with increasing section depth. However, what is most surprising is that the Y-shaped features persist at all with such deep sectioning. Typically, the width of the arms varies between 2-5 μm, wherein we would expect a conventional (cylindrical) dendrite visible in part (a) of the figure to have completely vanished by part (e). The primary conclusion from the serial sectioning must therefore be that the features being observed must be much more extensive in the direction normal to the plane of the section than their width in the plane of the section, essentially each arm having a sheet like morphology.

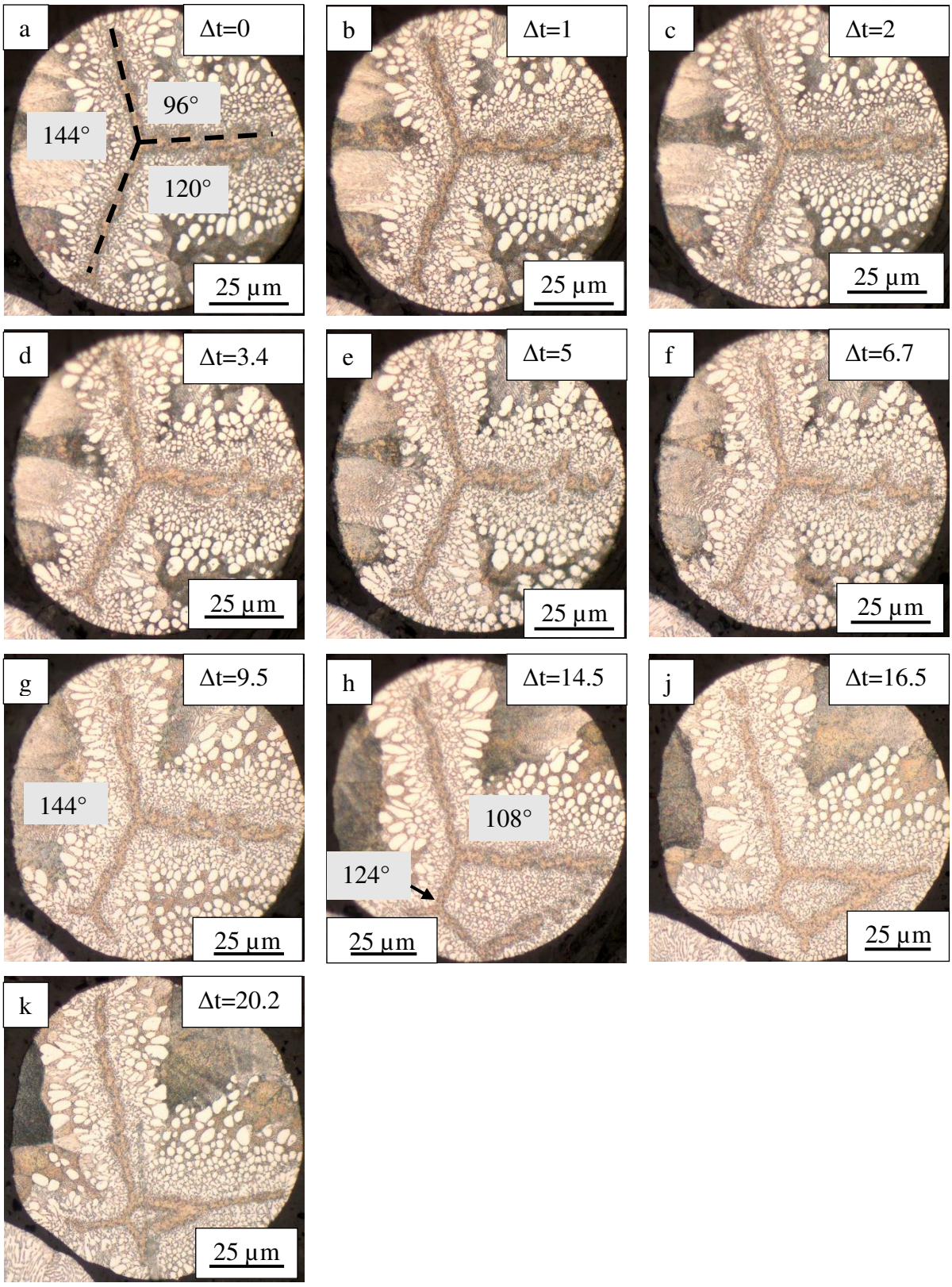

Figure 9: 3D structure of Y-shaped phase formed in 150-106 µm sample. Δt is the cumulative depth of the samples after polishing in µm.

Eutectic Spacing

The eutectic spacing of the lamellar eutectic was measured as a function of droplet size, the results being given in Figure 10. The eutectic spacing for the 850+ µm sample was measured as 1.3 µm and this figure decreased with increasing cooling rate to around 0.35 µm for the 300-212 µm sample. However, further increase in the cooling rate resulted in a slight increase in spacing to 0.45 µm in 212-150 µm sample. It must be noted here that this size fraction (212-150 µm) is the one in which the featureless Y-shaped structures first started to emerge. Thereafter, the spacing decreases again monotonically with decreasing particle size, although the eutectic spacing for the 150-106 µm sample remained slightly higher than that of the 300-212 µm sieve fraction. The smallest eutectic spacing was measured as 0.23 µm for 53-38 µm sample.

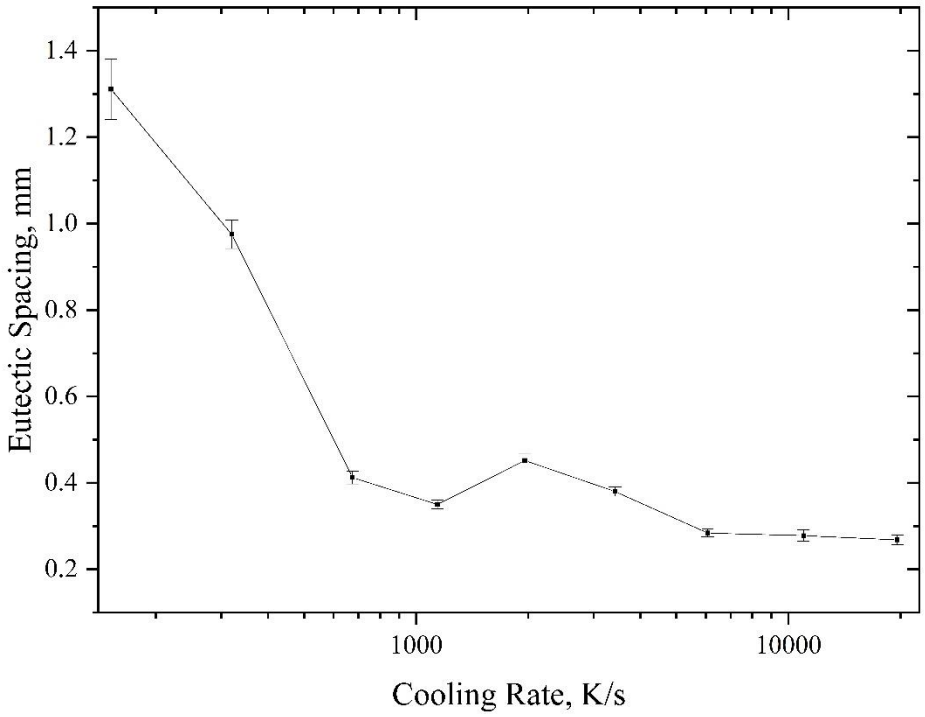

Figure 10: Eutectic spacing as a function of estimated cooling rate.

TEM analysis

A FIB cut sample from a Y-shaped region of 150-106 µm sample was further analysed using TEM in order to reveal the internal structure of this apparently featureless region, with the results being given in Figure 11. It was found that this region consists mostly of very fine spherical and needle-like precipitates. The diameters of the spherical precipitates range between 5 to 50 nm. The dimensions of the needle-like precipitates are of the order 5x50 nm.

However, there is, towards the bottom right-hand corner of the micrograph, a larger precipitate which appears to be surrounded by a halo of darker material largely free from precipitates. We will return to the consideration of this structure later. EDX mapping, given in Figures 11b & c show that these are iron rich precipitates. However, quantitative EDX measurements are not possible as the thickness of the precipitates is smaller than that of the TEM sample. Consequently, EDX results will not be accurate as the beam will sample both precipitate and matrix. Figure 11d & e shows the SAD pattern taken from Figure 11a. This has been analysed using both the d-spacings and the angles between the spot patterns. While the bright spot pattern shown in Figure 11d belongs to α-Al the weaker spot pattern in consistent with Al_mFe around a $[0\bar{1}0]$ zone axis. The SAD pattern in Figure 11e is also taken from Y-shaped region. This shows a distinct ring pattern, with such ring patterns indicating very fine polycrystalline structure, which would be consistent with the bright field micrograph (Figure 11a). The spot patterns on, or close to the ring pattern, belong to four strongest peaks of Al_mFe[18] with very close d-spacings; namely [307], [330], [413] and [321].

As seen from Figure 8, the "featureless" material that comprises the Y-shaped morphologies can also adopt a more conventional dendritic morphology and to ensure this is the same material a second FIB section from the dendrite-like region of a 53-38 µm sample was analysed under TEM. A bright-field image of this is shown in Figure 12, revealing that this region consists of a mixture of large Fe-rich (> 400 nm) precipitates surrounded by halos of Al matrix more-or-less free of precipitates with these being separated by wavy bands of material containing very fine spherical and needle-like precipitates. The structure within these wavy bands we believe to be the same as that occupying the majority of the micrograph in Figure 11 and that overall the structures shown in Figure 11 & 12 are similar, but with a higher density of the coarse precipitates being present in Figure 12, there only being one such coarse precipitate and halo in Figure 11, that in the bottom right-hand corner of the micrograph.

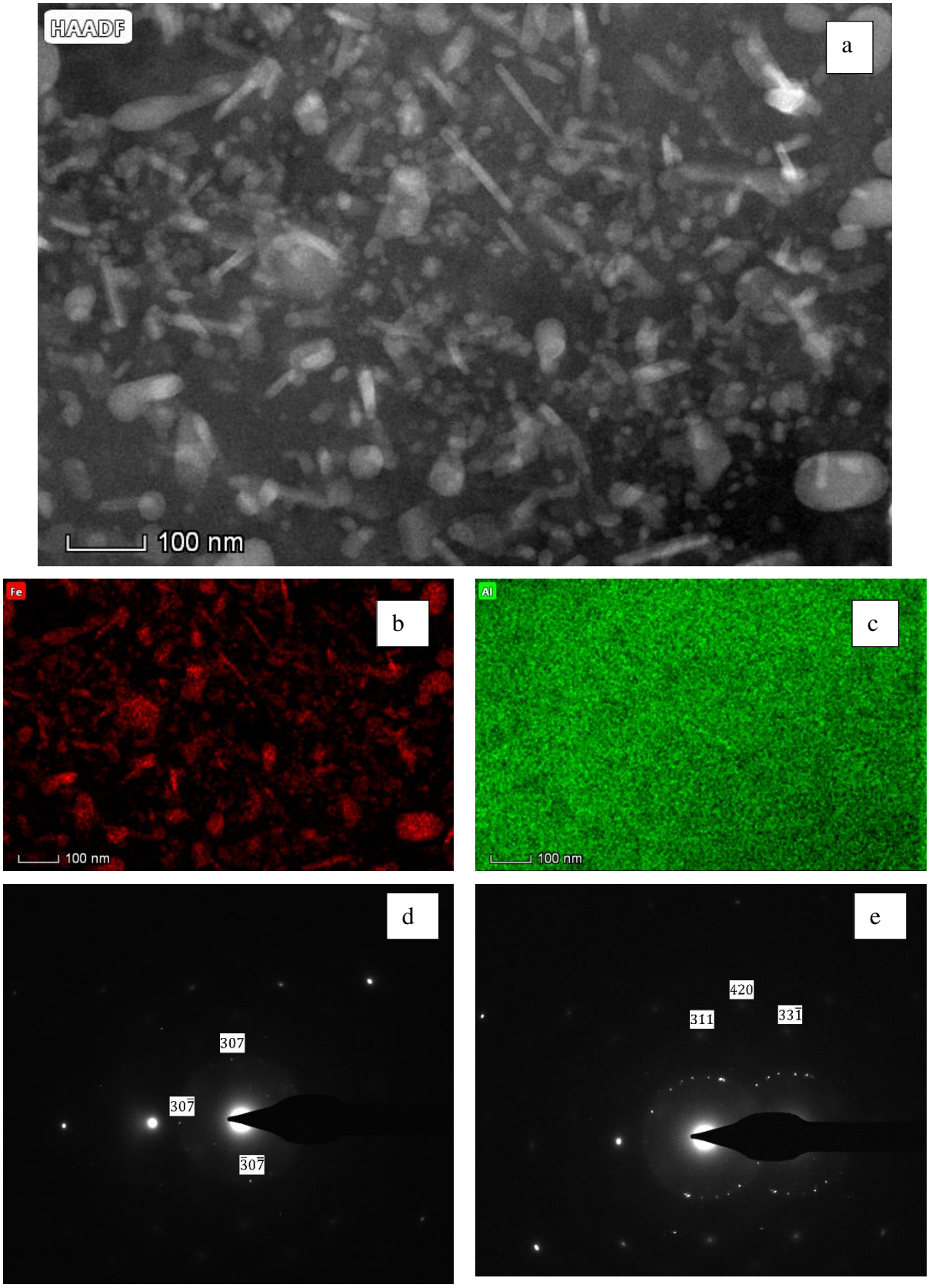

Figure 11: a) TEM micrograph of Y-shaped region showing nanosized spherical and needle-like precipitates, b) and c) EDX mapping of the region showing Fe and Al, respectively, d) SAD pattern taken from Y-shaped region showing Al_mFe taken from

$[0\bar{1}0]$ zone axis e) SAD pattern taken from Y-shaped region spot patterns on the ring pattern corresponds to four strongest peaks of Al_mFe.

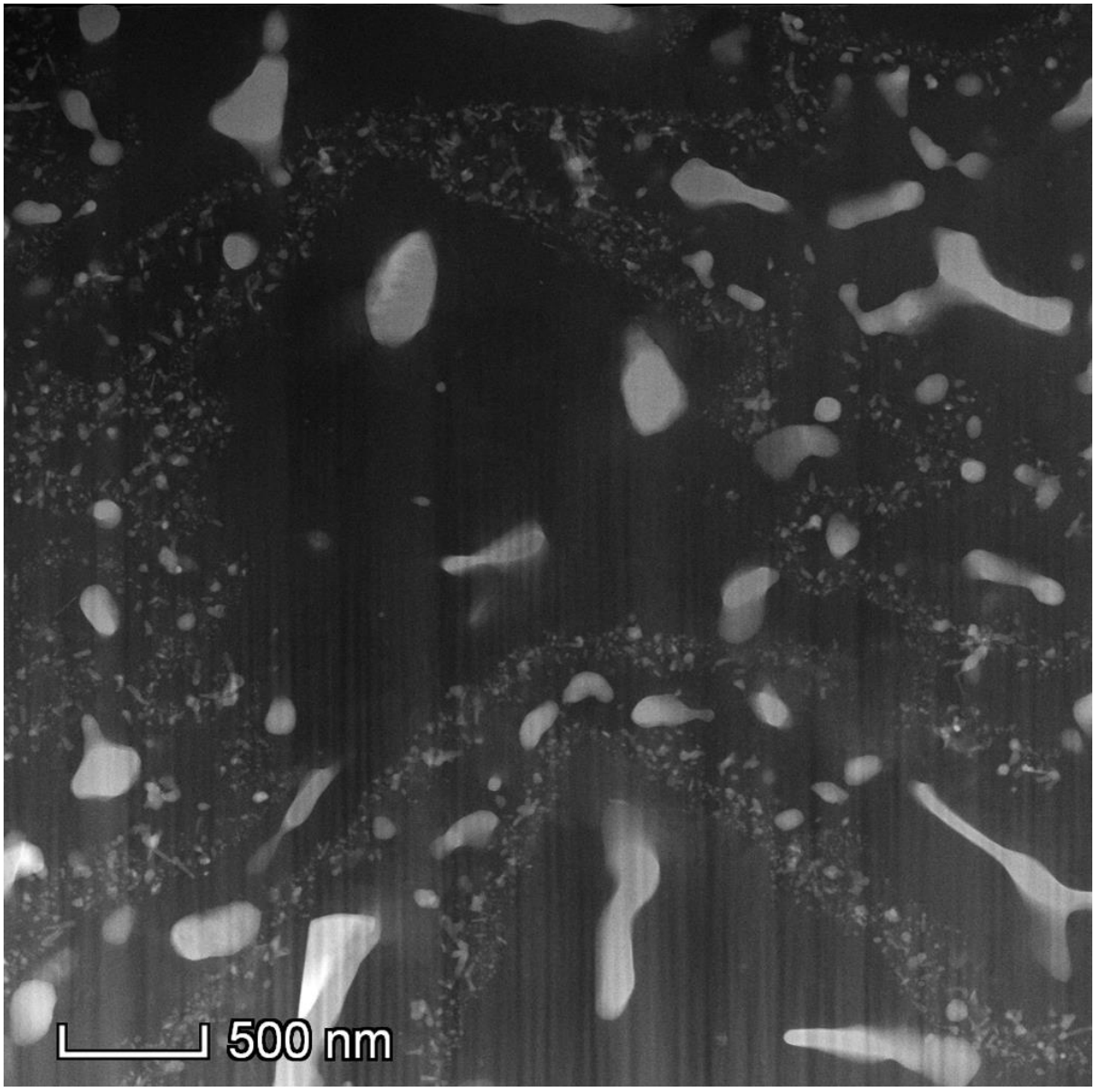

Figure 12: TEM micrograph taken from dendrite-like Y-shaped region of 53-38 µm sample.

3.4. Microhardness

In order to understand the effect of the non-equilibrium solidification on the mechanical properties of the alloy, Vickers microhardness measurement were employed on all sample fractions with a standard indenter using 10 g load and 10 s dwell time. 10 measurements were performed for each sample fraction and the results are given in Figure 13. Overall, the

microhardness of the alloy is gradually increasing with increasing cooling rate. The minimum microhardness was observed in the slowest cooled sample (850+ µm) as 50 $HV_{0.01}$ and this value rise to reach a maximum of 83 $HV_{0.01}$ in 53-38 µm sample. The total increase in the microhardness of the alloy is around 60%. This increase is likely due to the combined effect of increasing supersaturation and scale refinement[19], both of which will tend to increase the microhardness. It must be noted here that the microhardness value for 300-212 µm samples is slightly lower than 500-300 µm samples. This slight decrease happening one sieve size before the onset of Y-shaped crystal growth, where eutectic spacing starts to increase.

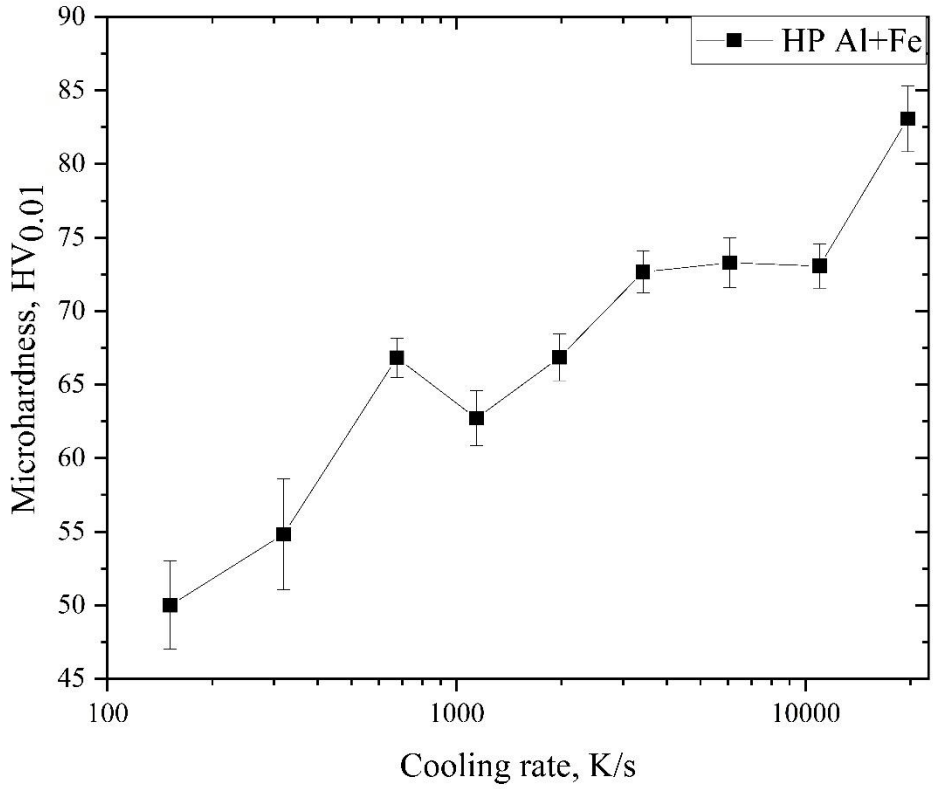

Figure 13: Microhardness value (in $HV_{0.01}$) as a function of cooling rate.

4. Discussion

An Al-3.9 wt% Fe alloy has been subjected to rapid solidification using a 6.5 m drop-tube with cooling rates ranging between 100 and 20000 K s^{-1} with a wide range of microstructure having been observed. Large powders (d > 212 µm) show the formation of blocky proeutectic $Al_{13}Fe_4$, both stable Al-$Al_{13}Fe_4$ and metastable Al-Al_6Fe eutectics and dendritic α-Al (Figure

4), leading to a complex, but understandable, solidification sequence. Most samples display the growth of proeutectic $Al_{13}Fe_4$, often surrounded by a halo α-Al without any eutectic. This is due to the local solute concentration being depleted in Fe during proeutetic growth, terminating the growth of this phase and permitting the growth of α-Al. Moreover, some samples also show regions displaying the growth of primary dendritic α-Al. Based upon the metastable phase diagram proposed in our previous work[15], Al-3.9 wt% Fe misses the coupled zone for the Al-$Al_{13}Fe_4$ eutectic in favour of primary α-Al growth if a minimum of undercooling of 110 K is attained. In addition, much of the sample is occupied by eutectic, this being both the stable Al-$Al_{13}Fe_4$ lamellar eutectic and the metastable Al-Al_6Fe rod-like eutectic. These often occur in adjacent, and closely mixed regions, meaning it is not possible to determine which grew first, or indeed whether both were growing simultaneously.

Decreasing the sample size, and thus increasing the cooling rate, results in drastic changes to the microstructure. Primary $Al_{13}Fe_4$ disappears in samples with d < 212 µm. This is likely due to competitive growth, with slow growing faceted phases, such as $Al_{13}Fe_4$, being outgrown at the higher cooling rates and deeper undercoolings experienced by the smaller droplets. This would tie on with the observed increase in eutectic spacing (Figure 10) in these smaller droplets. According to the Jackson and Hunt (JH) [20]model for eutectic growth, an increase in eutectic spacing indicates a decrease in both growth rate and undercooling in the eutectic. Our supposition is that the latent heat released during the slow growth of faceted $Al_{13}Fe_4$ represents a relatively small contribution to the overall heat budget for the droplet but that once this is replaced by the growth of more rapidly growing phases there is a much larger input of latent heat to the overall heat budget. The consequence is that the residual undercooling of the droplet, following growth of the primary phase, is therefore lower. As it is this residual undercooling that drives the eutectic growth, this will be manifest in a slight increase in the lamellar eutectic spacing. Based on a JH coefficient for the Al-$Al_{13}Fe_4$ lamellar eutectic of $\lambda\Delta T = 8.79$ µm K [21,22] this would correspond to a residual undercooling in the 300-212 µm droplet following proeutectic $Al_{13}Fe_4$ growth of 24.4 K compared to a residual undercooling in the 212-150 µm droplet following growth of the Y-shaped features and the dendritic α-Al of 19.6 K.

However, the most dramatic change in the solidification morphology is the emergence of what we have termed featureless Y-shaped morphologies which are observed in all samples with d < 212 µm. These adopt a wide range of geometries but, as shown in Figure 9, the basic unit seems to be that, in 2D projection, of three intersecting lines with near, but not exact,

120° intersections. As is clear from serial sectioning, these features which appear as lines in cross section are long in the direction normal to the section, meaning that in 3D they have the geometry of a plane sheet. Structures which appear to be similar have also been reported in impulse atomized hypoeutectic Al-0.61 wt% Fe and hypereutectic Al-1.90wt% Fe[23] and impulse atomized Al-5wt%Cu and Al-17wt%Cu[17].

In order to illustrate the 3D structure revealed by the serial sectioning we have produced a schematic reconstruction of the simple Y-shaped structure revealed in Figures 9a-g. By a schematic reconstruction we mean that the positions, intersections, angles and inclinations of the planes required to produce the serial sections have been accurately reproduced, but that no attempt has been made to capture the thickness or lateral structure of the planes. For instance, from Figure 9 it is evident that there is considerable variability in the width of the arms along their length and in particular that the L2 arm is both thicker and much more heavily fragmented than the other two main arms. The result of this reconstruction is given in Figure 14, with the diagram in approximately the same orientation and the serial sections in Figure 9. It is clear from the reconstruction that the main Y-structure shown in Figure 9a-g can be reconstructed from three intersecting planes, with a further two plane to produce the splitting of the L3 main arm. All three planes are close to orthogonal to the plane of the section, with the smallest deviation being for the L1 arm (0.9° from the normal to the section) and the largest for the L2 arm (2.7° from the normal to the section). This is consistent with the evolution of the Y-shaped structure with progressive sectioning. With reference to Figure 9 we note that the L1 arm remains approximately in its original position while the L2 arm drifts downwards due to the inclination of the plane. We also note that there is, in general, no reason why the sectioning plane should be orthogonal to the planar crystal sheets that comprise the Y-shaped features and we suspect that in picking a particularly simple Y-shaped structure to section we have effectively selected a droplet in which this condition is met. As an aside, we take this as the motivation for our nomenclature of Y-shaped features, the basic morphology being that of three intersecting planes in a three pronged “Y” and this is the morphology observed when sectioning (approximately) normal to the planes. When sectioning is not normal to the planes, more complex morphologies (closed shapes etc.) may be observed.

It is clear from the rest of the solidification morphology in the droplets that these featureless, intersecting planes are the primary solidification phase, with dendrites of α-Al radiating out from these features and becoming progressively coarser with increasing distance from them.

Moreover, the fortuitous observation of a droplet from the 106-75 µm sieve fraction with a much smaller satellite particle embedded within it (Figure 7a) reinforces this conclusion. It is clear from the morphology of the two particles at the impact site that the smaller particle was solid and the larger particle (at least partially) liquid as the time of impact. As such, the smaller particle would be expected to act as a heterogeneous nucleant, with the solidification front propagating outwards from the impact site. That the material immediately adjacent to the impact zone in the large droplet is this same, Fe-rich, featureless phase is clear evidence for this being the primary solidification phase.

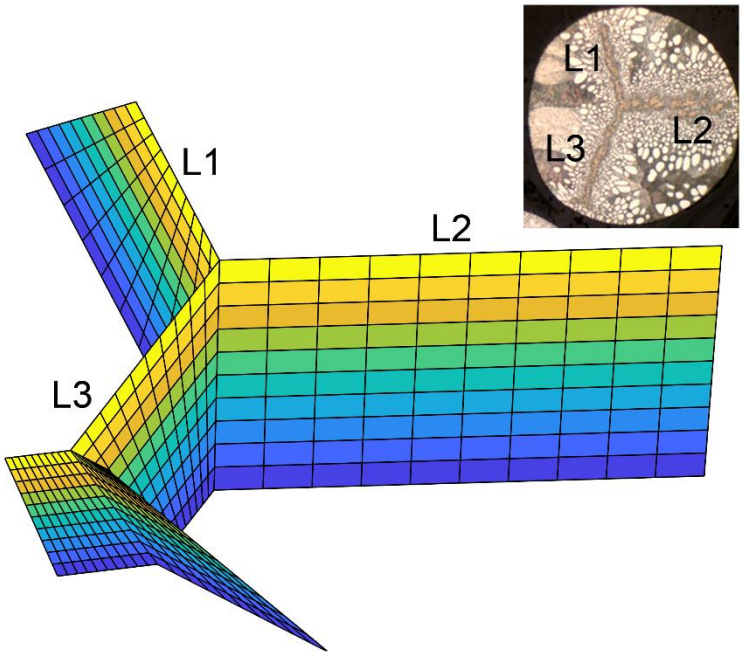

Figure 14: Schematic reconstruction of the internal structure of the droplet giving rise to the serial sectioning shown in Figure 9a-g. The Y-shaped structure is composed of three intersecting planes almost orthogonal to the sectioning plane.

Moving further away from the Y-shaped features we then see the growth of both Al-$Al_{13}Fe_4$ eutectic and Al-Al_6Fe eutectic. Tentative evidence suggests that the stable Al-$Al_{13}Fe_4$ eutectic grows first as this generally forms closer to the dendritic regions, with the Al-Al_6Fe eutectic forming on the margins of the droplets. This may seem anomalous, but we believe that following recalescence, particularly for the fast growing dendritic phase, the droplet may be close to the eutectic temperature, favouring the growth of the stable eutectic. However, as eutectic growth is slow, the macroscopic heat extraction rate may exceed that of latent heat

generation, leading to the droplet cooling post-recalescence so that the metastable eutectic is favoured towards the end of solidification.

In the smallest droplets Y-shaped feature appear less common and dendrites appear more common. However, it is not yet clear whether these are true (cylindrical) dendrites or whether they have the same sheet like extension into the sample as we believe to be the case for the Y-shaped features. Figure 7d shows the formation of both needle-like and spherical precipitates in the centre of, and perfectly aligned with, a dendrite trunk. The most natural explanation of such a line of precipitates would seem to be the growth of a thin rod or sheet of intermetallic which then underwent partial fragmentation and spheroidisation whilst in co-existence with the liquid before nucleating the "featureless" phase. Such post-recalescence fragmentation and spheroidisation of a primary solidification phase during drop-tube processing has previously been reported in congruently melting Ni-Ge intermetallics[24].

During SEM analysis the material comprising the Y-shaped feature appears featureless, with a composition close to that of the original liquid, namely 3.9 wt% Fe. Under the TEM this material comprises an α-Al matrix embedded within which are numerous Fe-rich spherical and needle like precipitates. Some of these are relatively coarse, and where this is the case they are surrounded by a halo of α-Al devoid of other precipitates. Elsewhere much finer precipitates are observed and these tend to occur in bands. Analysis of SAD data from the TEM suggests that these are most likely of the metastable phase Al_mFe. This seem plausible given that Al_mFe has been shown to form both direct from the melt at high solidification rates[9,25] and via solid-state decomposition in Al-Fe alloys that have experienced high growth rates[18].

The size of these finer precipitates, 5-50 nm diameter for the spherical precipitates and 5×50 nm for the needles, is indicative of formation via a solid-state reaction, rather than direct growth from the liquid. However, the precipitates do not display strongly faceted interfaces and there is little evidence for preferred growth directions, both of which would be expected for precipitates forming via a solid-state decomposition, and so this conclusion remains conjectural. We believe that the most likely scenario is that the coarse particulates formed direct from the liquid, possibly as either a continuous rod or sheet which subsequently fragmented before nucleating the precursor of the featureless phase, which itself then underwent a solid-state decomposition to α-Al and Al_mFe. In this regard, an $NiSn_4$

intermetallic has previously been observed to display a similar behaviour, growing as a plane sheet which transforms to a (faceted) dendrite as the cooling rate is increased[26].

In terms of a solidification sequence for these smaller droplets we believe that this began with the growth of an intermetallic, probably Al_mFe, growing either as fine needle dendrites or a thin planar sheet, both of which would likely have been subject to fragmentation and spheroidisation soon after growth. This intermetallic would then have initiated the growth of the "featureless" material comprising the Y-shaped features. Given that the structure revealed in the TEM and the EDX results which show that this material has the same composition as the liquid, we conjecture that this was highly supersaturated α-Al, growing via partitionless (or near partitionless) solidification. For Al-3.9 wt% Fe, T_0 temperature has been calculated, using standard CALPHAD methods and assessed thermodynamic data for Al-Fe as given by Liu & Chang[27] as 42 K below the Al-$Al_{13}Fe_4$ eutectic. This is eminently achievable in the drop tube and in fact rather less than the undercooling determined experimentally to bypass the coupled zone for Al-$Al_{13}Fe_4$ eutectic growth. We suspect therefore that partitionless growth of α-Al is actually achieved at rather higher undercoolings than suggested by the T_0 temperature and once the eutectic coupled zone has been bypassed. Due to its extremely metastable nature this highly supersaturated α-Al would then have undergone solid-state decomposition into the observed structure of fine nanoscale precipitates of Al_mFe in a less supersaturated α matrix. Such growth, being limited only by thermal diffusion, would initially have been very rapid, possibly as a plane front parallel to the plane of the initiating intermetallic. However, noting there is no steady-state solution for diffusion at a plane front, such growth would have rapidly slowed due to warming of the droplet, thereby transitioning into the growth of dendritic α-Al, which would have been supersaturated in Fe, but not partitionless. Warming of the droplet therefore continues as growth proceeds, leading to a continuous coarsening of the primary dendrites arms, which would not be expected during growth of dendrites from a point nucleation site but must be a consequence of nucleation on a plane. Finally, with a further drop in the undercooling solidification is terminated with growth of the Al-$Al_{13}Fe_4$ and Al-Al_6Fe eutectics.

5. Acknowledgements

Corresponding author would like to thank the Republic of Turkey Ministry of National Education, Directorate General for Higher and Overseas Education for their support. The authors gratefully acknowledge LEMAS for their support & assistance in this work

6. References

1. Liu W, Yang J, Xiao B. Application of Bayer red mud for iron recovery and building material production from alumosilicate residues. J Hazard Mater. 2009;161(1):474–8.

2. Zhang L, Gao J, Damoah LNW, Robertson DG. Removal of iron from aluminum: A review. Miner Process Extr Metall Rev. 2012;33(2):99–157.

3. Nayak SS, Chang HJ, Kim DH, Pabi SK, Murty BS. Formation of metastable phases and nanocomposite structures in rapidly solidified Al-Fe alloys. Mater Sci Eng A. 2011;528(18):5967–73.

4. Cotton JD, Kaufman MJ. Microstructural evolution in rapidly solidified Al-Fe alloys: An alternative explanation. Metall Trans A. 1991;22(4):927–34.

5. Çadırlı E, Herlach DM, Volkmann T. Characterization of rapidly solidified Ni–Si and Co–Al eutectic alloys in drop tube. J Non Cryst Solids. 2010;356(9–10):461–6.

6. Skinner DJ, Okazaki K, Adam CM. Physical Metallurgy and Mechanical Properties of Aluminum Alloys Containing Eight to Twelve Weight Percent Iron. Rapidly Solidified Powder Alum Alloy. 1986;

7. Chen J, Lengsdorf R, Henein H, Herlach DM, Dahlborg U, Calvo-Dahlborg M. Microstructure evolution in undercooled Al–8 wt% Fe melts: Comparison between terrestrial and parabolic flight conditions. J Alloys Compd. 2013;556:243–51.

8. Chen J, Dahlborg U, Bao CM, Calvo-Dahlborg M, Henein H. Microstructure evolution of atomized Al-0.61 wt pct Fe and Al-1.90 wt pct Fe alloys. Metall Mater Trans B. 2011;42(3):557–67.

9. Young RMK, Clyne TW. An AlmFe intermetallic phase formed during controlled solidification. Scr Metall. 1981;15(11):1211–6.

10. Mullis AM, Bigg TD, Adkins NJ. A microstructural investigation of gas atomized Raney type Al-27.5 at.% Ni catalyst precursor alloys. J Alloys Compd. 2015;648:139–48.

11. Li S, Wu P, Fukuda H, Ando T. Simulation of the solidification of gas-atomized Sn-5mass%Pb droplets. Mater Sci Eng A. 2009;499(1–2):396–403.

12. Boettinger WJ, Bendersky L, Early JG. An analysis of the microstructure of rapidly solidified Al-8 wt pct Fe powder. Metall Trans A. 1986;17(5):781–90.

13. Cochrane RF, Evans P V, Greer AL. Competitive growth analysis of phase formation in Al-8wt.% Fe. Mater Sci Eng A. 1991;133:803–6.

14. Sharma SC, Volkmann T, Herlach DM. Microstructural development in drop-tube-solidified Al-3.6 wt.% Fe droplets: an analysis. Mater Sci Eng A. 1993;171(1–2):169–73.

15. Abul MR, Cochrane RF, Mullis AM. Microstructural Development and Mechanical Properties of Drop Tube Atomized Al-2.85 wt% Fe. J Mater Sci Technol. 2021;

16. Henein H, Buchoud V, Schmidt RR, Watt C, Malakhor D, Gandin CA, et al. Droplet solidification of impulse atomized Al-0.61Fe and Al-1.9Fe. Can Metall Q. 2010;49(3):275–92.

17. Prasad A, Henein H, Maire E, Gandin C-A. X-ray tomography study of atomized Al-Cu droplets. Can Metall Q. 2004;43(2):273–82.

18. Aliravci A. Kinetics, thermodynamics and mechanism of metastable Al-AlmFe phase and fir-tree zone formation in DC-cast Al-Fe-Si alloy ingots. 2006;

19. Ruan Y, Wang XJ, Chang S-Y. Two hardening mechanisms in high-level undercooled Al–Cu–Ge alloys. Acta Mater. 2015;91:183–91.

20. Jackson KA. Hunt. JD Lamellar and rod eutectic growth. Trans AIME. 1966;236:1129–42.

21. Lü P, Wang HP. Observation of the transition from primary dendrites to coupled growth induced by undercooling within NiZr hyperperitectic alloy. Scr Mater. 2017;137:31–5.

22. Liang D, Jones H. The effect of growth velocity on growth temperature of the Al-Al3Fe and Al-Al6Fe eutectics. Zeitschrift für Met. 1992;83(4):224–6.

23. Henein H, Buchoud V, Schmidt R-R, Watt C, Malakov D, Gandin C-A, et al. Droplet solidification of impulse atomized Al-0.61 Fe and Al-1.9 Fe. Can Metall Q. 2010;49(3):275–92.

24. Mullis AM, Haque N. Evidence for dendritic fragmentation in as-solidified samples of deeply undercooled melts. J Cryst Growth. 2020;529:125276.

25. Griger A, Stefániay V, Kovács-Cseténvi E, Turmezey T. Formation and transformation of binary intermetallic phases in high purity Al-Fe alloys. In: Key Engineering Materials. Trans Tech Publ; 1990. p. 17–30.

26. Belyakov SA, Gourlay CM. NiSn4 formation during the solidification of Sn–Ni alloys. Intermetallics. 2012;25:48–59.

27. Liu Z-K, Chang YA. Thermodynamic assessment of the Al-Fe-Si system. Metall Mater Trans A. 1999;30(4):1081–95.